

Davide Mazza, Alice Abernathy, Nicole Golob, Tatsuya Morisaki and James G McNally

Supplementary Information for “ A benchmark for chromatin binding measurements in live cells”

Table of contents:

Supplementary Results. Validation of HaloTag constructs.

Supplementary Methods. SMT Microscopy; Fluorescence recovery after photobleaching and fluorescence correlation spectroscopy; Monte Carlo Simulations; Measurement of diffusion time through FRAP and FCS volumes.

Supplementary Note. Derivation of kinetic models for the SMT histograms of displacements.
displacements obtained at different frame rates.

Supplementary Figure 1. Characterization of HaloTag p53-wt photostability and dynamics.

Supplementary Figure 2. Details of the microscope for SMT.

Supplementary Figure 3. Dependence of the measured residence time on the selection of thresholds and on the photobleaching rate

Supplementary Figure 4. Fitting of the H2B displacement histogram at multiple time points.

Supplementary Figure 5. Fitting of the p53-wt displacement histogram at multiple time points.

Supplementary Figure 6. FRAP estimates of the p53-wt residence time depend on the bleach spot size.

Supplementary Figure 7. Validation of the SMT kinetic model by simulations.

Supplementary Table 1. Estimates of p53 binding rates from kinetic modelling of the histogram of

Supplementary Movie Legends 1-2.

Supplementary Results.

Validation of the HaloTag-constructs for SMT experiments.

As we described in the main text we constructed a fluorescently tagged version of p53 that was genetically encoded and photostable, by fusing p53 to the HaloTag (1) motif. Immobilized Halotag p53 fusion proteins in fixed cells displayed the characteristic one-step photobleaching (Supplementary Fig. 1a), indicating that we were observing individual molecules with our custom-built widefield microscope with an inclined illumination scheme (Supplementary Fig. 2). Occasionally (<5%), multi-step photobleaching was observed, compatible with having two or more of the four molecules in the p53 tetramer labeled with the HaloTag ligand. In living cells we also observed sudden disappearance of the tracked fluorescent spots (See Supplementary Movies 1 and 2). Furthermore, we measured similar fluorescent intensities from the detected diffraction-limited spots in fixed and living cells, also indicating that individual molecules were observed (Supplementary Fig. 1b).

We found that the Halotag-TMR was much more photostable than GFP (Supplementary Fig. 1c). Also, we found that the Halotag fusion did not disrupt p53 kinetics, as FRAP and FCS curves were similar to those obtained with a previously characterized (2) p53-wt-GFP fusion protein (Supplementary Fig. 1d and e). The single molecule tracks obtained with the Halotag fusion reflected movement of the fusion protein and were not due to movement of free Halotag-TMR, since cells treated with the Halotag-TMR labeling protocol but not transfected with the Halotag p53 fusion showed none of the tracks seen in the cells containing the fusion protein (Supplementary Fig. 1f).

We determined the fraction of Halotag p53 molecules that were labeled by the HaloTag-TMR ligand by measuring the total fluorescence intensity in the nucleus of H1299 cells as a function of the ligand concentration added to the cell medium. We found that for ligand concentrations higher than 1 μ M a plateau was reached corresponding to an ~100% labeled fraction, but lower ligand concentrations produced progressively lower labeled fractions as measured by decreases in average cell brightness (Supplementary Fig. 1g). By fitting a smooth curve through these calibration measurements, we calculated a p53 labeled fraction of ~79% for FRAP, 28% for FCS and 4% for SMT based on the different ligand concentrations of 500 nM, 50 nM and 5 nM that we used for these three different modalities. From the SMT labeled fraction of 4% we can roughly estimate the total number of transfected p53 molecules (both labeled and unlabeled) in the H1299 p53-null cells. Our SMT movies showed 5 to 30 molecules per image, and since this represents a 4% labeled fraction, there must have been from 125 to 750 total p53 molecules in the focal plane. The detection slice in SMT is ~1.5 μ m thick, which is roughly one fifth of the total nuclear volume. Thus 5x 125-750 or 600 to 4000 transfected p53 molecules were present in the cells.

Supplementary Methods

SMT Microscopy

Single molecule tracking was performed on a custom-built widefield fluorescence microscope with a highly inclined illumination scheme (3). The excitation beam, a 25mW 561 nm laser (details of the excitation path are given in Supplementary Fig. 2), was delivered to the back port of an Olympus IX-81 inverted microscope (Olympus Corp., Center Valley, PA) and focused on the back aperture of the objective (a 150x, NA 1.45 oil immersion objective). A field stop was used to limit the excitation to an area of approximately 15µm in diameter. The inclination of the beam was selected to be approximately 60° from the optical axis at the oil-coverslip interface. The sample was mounted on a piezoelectric stage (Physik Instrumente, Auborn, MA) enabling selection of the focal plane without modifying the position of the objective. The focal plane was chosen to lie in a middle section of the cell nucleus, at a depth of 3 to 4 µm from the position of the coverslip. For every cell, a time-series composed of 400 images was collected.

The EM-CCD (Cascade 512B, Photometrics, Tucson, AZ) camera and the laser source were synchronized by means of a pulse generator (BNC-575, Berkeley Nucleonics, San Rafael, CA) in order to avoid photobleaching when the camera shutter was closed (exposure times were set to 10 ms). To compare the histograms of displacements between p53-wt, p53-d30 and p53-R273H a fast acquisition rate of 50Hz was used, while the distribution of residence times was also collected with slower acquisition rates (25Hz and 10Hz) in order to test the effect of photobleaching (See Supplementary Table 1 and Supplementary Fig. 3b). An irradiation intensity of 0.8 kW/cm² was used. The sample was kept at 37°C with an air-stream stage incubator (Nevtek, Burnsville, VA). Exemplary acquisitions for p53-wt and for the H2B constructs are provided in Supplementary Movie 1 and 2 respectively.

The collected movies were analyzed by custom-written Matlab (Mathworks, Natick, MA) routines to identify and track individual molecules. First, the images were processed with a band-pass filter, with a lower threshold of 1 pixel (0.104 nm) and higher threshold of 5 pixels both to smooth the diffraction limited spots corresponding to single molecules and to suppress pixel noise. A peak identification algorithm was then used to identify the individual molecules and a lower intensity threshold (set to 150 AU) was used to discard dim peak intensities corresponding to out-of-focus molecules. The sub-pixel localization of the single molecule was then determined by fitting two-dimensional Gaussians to the unprocessed images using the previously identified peak coordinates as starting guesses. The coordinates of the identified molecules at different frames were linked into tracks using the Matlab version of the Crocker and Weeks algorithm (4). We allowed for a maximum displacement between contiguous frames equal to 12 pixels (1.25 µm) for p53-wt and 4 pixels (0.42 µm) for H2B and we discarded tracks shorter than 3 frames. All trajectories were manually inspected to minimize mistracking.

Fluorescence Recovery after Photobleaching and Fluorescence Correlation Spectroscopy.

FRAP and FCS were performed on a Zeiss 510 Live DuoScan confocal microscope equipped with a 63x /1.4 NA oil immersion objective (Carl Zeiss Inc., Thornwood, NY). A 488 nm/100mW diode laser and a 561 nm/50 mW DPSS laser were used to image the GFP and the Halo-TMR labeled constructs respectively. Both FRAP and FCS experiments were performed on homogeneous regions of the cell

nucleus, as far as possible from the nuclear boundary and nucleoli. Cells were kept at 37 °C and 5% CO₂ concentration by means of a stage incubator.

FRAP data were collected by acquiring 100 prebleach images (200x200 pixels², pixel size = 0.104 μm², pinhole 2.5 Airy units corresponding to a 2.0 μm optical slice, AOTF 1 to 5%) at a frame rate of 30 Hz, followed by the photobleach of a circular region with the 488 nm laser line (AOTF 100% for the Halo-TMR labeled constructs and AOTF 30% for the GFP-labeled constructs). The time for the bleach iteration ranged from 10 to 90 ms depending on the size of the bleach region. After the bleach, the fluorescence recovery was followed for 900 frames with the same settings used for the prebleach time series. The collected images were registered to correct for cell movement, background subtracted and corrected for observational photobleaching by normalizing for the total nuclear intensity at the first postbleach frame. The curves were logarithmically binned to avoid overweighting of the last part of the fluorescence recovery.

FCS data were collected according to a TICS (Temporal Image Correlation Spectroscopy) protocol (5) in which the temporal autocorrelation curves are computed from multiple pixels of an image sequence and averaged together to provide estimates for the kinetic parameters of a single cell. The calibration of the observation volume was performed as in (5). The FCS/TICS data were obtained by repeatedly imaging a line of 200 pixels in width and 1 pixel in height at 500Hz for 100s. The pixel size was chosen equal to 210 nm. The fluorescence intensity time-course was corrected for photobleaching by subtracting a double-exponential decay trend line. A bias equal to the fluorescence intensity recorded at the first time-point was added to the whole time series in order to preserve the information about the number of molecules. Data showing artifacts arising from cell motion were discarded. The fluorescence fluctuations were then autocorrelated via fast Fourier transform and the autocorrelation curves from different pixels of the same cell were averaged together.

The FRAP and FCS data were then analyzed with a two binding state model (no diffusion), with a one binding and one diffusing state model and with a two diffusion component model with custom written Matlab routines as described in (6, 7).

Although a two state diffusion model has been widely used in FCS, it has not been widely applied in FRAP. The FRAP version of this model that we used was:

$$frap_{D2}(t) = f_1 frap_D(t, D_1) + (1 - f_1) frap_D(t, D_2)$$

where $frap_D(t, D)$ represents the expression for the FRAP recovery of a species with diffusion coefficient D (Equation 9 in (6)) and f_1 is the fraction of molecules with diffusion coefficient D_1 . As the slow fraction has been traditionally associated with bound molecules, we interpreted f_1 as the fraction of bound molecules, C_{eq} , when $D_1 < D_2$. Similarly, although a two-state binding model has been widely used in FRAP, it has not been used in FCS. The FCS version of this model that we used was:

$$f_{CSB2}(t) = \frac{1}{2^{3/2}N} (f_1 e^{-k_{off,1}t} + (1 - f_1) e^{-k_{off,2}t})$$

where N is the number of molecules in the observation volume, $k_{off,1}$ and $k_{off,2}$ are the dissociation rates for each of the two binding species and f_1 is the fraction of molecules with dissociation rate $k_{off,1}$.

Monte Carlo simulations of the effect of hindered diffusion in FRAP

To verify the effect of hindered diffusion in the FRAP estimates of binding we generated simulated FRAP curves via two-dimensional Monte Carlo simulations for an inert (non-binding) tracer diffusing through a crowded environment. The details of the simulations are as follows: we placed immobile obstacles at some fraction (below the percolation threshold, 42% for a square lattice) of the $10^3 \times 10^3$ nodes of a square lattice. The fraction was adjusted in different simulations to simulate different degrees of crowding. At the beginning of each simulation, we placed fluorescent molecules at 10^4 randomly selected lattice nodes that were not occupied by obstacles. We set the diffusion coefficient to $D_f = 1$ and the distance between the nodes to $r_{nodes} = 10\text{nm}$. This defined the time step between simulation updates as $r_{nodes}^2 / 4D_f$. The distance between the nodes was chosen to provide a reasonable size for the obstacles (10nm as in the beads on a string organization of chromatin). At each time step, we allowed all the particles to move off their nodes in a randomly chosen direction. We rejected moves if the new position of the particle corresponded to a node occupied by an obstacle. We repeated this procedure for 3×10^5 time steps to allow the system to equilibrate. Then we simulated the photobleach by coloring 90% of the molecules black in circles of different radii (0.5 to 1.5 μm) corresponding to FRAPs for different bleach-spot sizes. Following a simulated bleach at a given spot size, we let the system evolve for 10^6 time points to simulate the fluorescence recovery. Every 10^3 time steps we created a FRAP image by counting the number of non-bleached molecules in each of the $10^2 \times 10^2$ pixels obtained by binning 10×10 nodes together. We repeated this simulation ten times and averaged the fluorescence recovery images at each time point together. The averaged images were then analyzed as described above to obtain a FRAP recovery curve, and the resultant curves were fit with different kinetic models. The simulation results are reported in Supplementary Fig. 7.

Measurement of the diffusion time through the typical FCS and FRAP volume.

To quantify the time a free molecule takes to diffuse across the typical FRAP and FCS observation volumes, we calculated an average mean-squared displacement to traverse the FRAP and FCS measurement zone based on its dimensions w_x, w_y, w_z : $w_{avg}^2 = (w_x^2 + w_y^2 + w_z^2)/3$, with $w_x = w_y = 1 \mu\text{m}$, $w_z = 2 \mu\text{m}$ for the FRAP bleach spot and $w_x = w_y = 0.35 \mu\text{m}$, $w_z = 1 \mu\text{m}$ for the FCS focal volume. The time to traverse these average mean-squared-displacements was then determined by extrapolating the MSD plot obtained from the single molecule tracks corresponding to unbound molecules. As described in the main text, this yielded diffusion times of $\tau_{D,FRAP} = 0.28 \text{ s}$ and $\tau_{D,FCS} = 0.07 \text{ s}$ (see Fig. 3b in the main text).

These diffusion times were then compared to the time to bind a site τ_s , which is given by $\tau_s = \tau_b(1/C_{eq} - 1)$, where τ_b is the residence time and C_{eq} is the fraction of bound molecules. Our objective thresholding procedure of the SMT data yields estimates of $\tau_b = 1.7 \text{ s}$ and $C_{eq} = 19\%$, which then yields $\tau_s \sim 7 \text{ s}$.

Supplementary Note: Derivation of kinetic models for the SMT histograms of displacements

In this section we derive mathematical models to describe the distribution of displacements measured by single molecule tracking. We first describe the solution to the problem for the simpler case of one component diffusion and binding, and we then extend the solution to the case of multi-component diffusion and binding.

Brownian diffusion for free and bound molecules.

Traditionally, the histogram of displacements for nuclear proteins has been derived for a single molecule that is subject only to diffusion. The derivation requires a propagator $\varphi(\vec{r}, t)$ for diffusion, which is defined as the probability that a molecule starting at the origin will be at position \vec{r} at time t . For simple diffusion in two dimensions (8):

$$\varphi(\vec{r}, t) = (1/4\pi Dt) \exp(-r^2/4Dt) = (1/4\pi Dt) \exp(-(x^2 + y^2)/4Dt)$$

Equation S. 1

where D is the diffusion constant. The histogram of displacements is obtained by integrating this propagator over the circular shell of width Δr (where Δr is the bin size of the histogram):

$$p_D(r, t) \Delta r = \Delta r \int_0^{2\pi} r \varphi(\vec{r}, t) d\theta = \frac{2\pi r \Delta r}{4\pi Dt} e^{-\frac{r^2}{4Dt}}$$

Equation S. 2

Note that we use the letter “p” to denote the histogram of displacements because it corresponds to a probability, namely the probability of observing a molecule jumping a distance between $r - \Delta r/2$ and $r + \Delta r/2$ in a time t .

Previously, most single molecule data from cells have been fit assuming the motion can be described by one or more diffusing components. However, this approach does not directly account for the underlying dynamics of binding to a scaffold that diffuses much more slowly. This has been considered in one single molecule study, where numerical methods were developed to account for binding combined with simple 2D diffusion (9). Here, we develop more general analytical formulas for histograms of displacement in which molecules can alternate between a scaffold-bound state and a scaffold-free state while diffusing in three dimensions. This approach can be extended to include multi-component diffusion (see below) and to more accurately account for the experimental nature of single molecule detection within an optical section by allowing for three-dimensional diffusion that can only be detected within a finite z thickness.

The first step in deriving the new formulas is to consider how to account for a displacement r that can arise after a time t during which a molecule may have alternated multiple times between the scaffold-bound and the scaffold-free states. For the case of Brownian diffusion, motion in either state is independent of previous motion and we can merge together the time increments in the free state during which the molecule has moved a total distance \vec{r}' and treat it as a single time t' (which must be less than t), and correspondingly add up the time increments in the bound state during which the particle has moved a total distance $\vec{r} - \vec{r}'$ and treat it also as a single time $t - t'$. The resultant

displacement probability $I(r, t, t')$ is given by the product of the propagators of the free and bound states integrated over all the possible combinations of distances while free and bound and over a circular shell of width Δr :

$$I(r, t, t') = \Delta r \int_0^{2\pi} r d\theta \int_{-\infty}^{+\infty} d^2 \vec{r}' \varphi_f(\vec{r}', t') \varphi_b(\vec{r} - \vec{r}', t - t')$$

Equation S. 3

For the case of simple diffusion, the propagators for free and bound molecules are Gaussians (See Eq. S.1), and the expression for $I(r, t, t')$ therefore becomes the convolution of two Gaussians, which is itself a Gaussian, with variance given by the sum of the variances:

$$\begin{aligned} I(r, t, t') &= \frac{\Delta r}{4\pi D_f t'} \frac{1}{4\pi D_b (t - t')} \int_0^{2\pi} r d\theta \int_{-\infty}^{+\infty} dx' e^{-\frac{x'^2}{4D_f t'}} e^{-\frac{(x-x')^2}{4D_b (t-t')}} \int_{-\infty}^{+\infty} dy' e^{-\frac{y'^2}{4D_f t'}} e^{-\frac{(y-y')^2}{4D_b (t-t')}} \\ &= \frac{r \Delta r}{2(D_f t' + D_b (t - t'))} e^{-\frac{r^2}{4(D_f t' + D_b (t - t'))}} \end{aligned}$$

Equation S. 4

To obtain the histogram of displacements, this displacement probability $I(r, t, t')$ must be modulated by a function accounting for the probability that the molecule will be free for a time t' and bound for a time $t - t'$. This function $g(t', t)$ has been previously calculated for fluorescence correlation spectroscopy for transitions between a free state and a bound state governed by one-state, Poissonian distributed association and dissociation reactions (10):

$$\begin{aligned} g(t', t) &= C_{eq} e^{-k_{off} t} \delta(t') + (1 - C_{eq}) e^{-k_{on}^* t'} \delta(t - t') + \\ &\sum_{m=1}^{+\infty} \frac{(k_{on}^* k_{off})^m}{k_{on}^* + k_{off}} \frac{(k_{off} t' + k_{on}^* (t - t') + 2m)}{m! (m - 1)!} e^{-k_{on}^* t' - k_{off} (t - t')} (t' (t - t'))^{m-1} \end{aligned}$$

Equation S. 5

where k_{on}^* and k_{off} are the binding association and dissociation rates, δ represents a Dirac's delta and $C_{eq} = k_{on}^* / (k_{on}^* + k_{off})$ is the steady state probability of having a bound molecule. Note that the first and the second terms of $g(t', t)$ describe the probability of having the molecule respectively bound or free for the entire time t , while the sum represents all the intermediate situations. Specifically, each of the terms identified by a different index m corresponds to the probability of having m transitions between the free and the bound state. Thus the general solution for the histogram of displacements for a molecule alternating between the two states is given by the combination of Equation S.4 and S.5:

$$p(r, t) \Delta r = \int_0^t g(t', t) I(r, t, t') dt'$$

Equation S. 6

The last step in deriving the formula is to account for the fact that the experimental displacements are obtained from only a single focal plane of thickness Δz , since molecules diffusing out of this detection slice are no longer visible. As the observation time increases the probability of molecules exiting the slice increases, and this results in a histogram of displacements that decreases over time. To account for this loss we modify the equation for the histogram of displacements Equation S.6 with a correction term $\omega_f(\Delta z, t')$:

$$p(r, t) \Delta r = \int_0^t g(t', t) I(r, t, t') \omega_f(\Delta z, t') dt'$$

Equation S. 7

For simple diffusion, the probability $\omega_f(\Delta z, t')$ that a single molecule will stay in focus while freely diffusing for a time t' , can be calculated by assuming absorbing boundaries at the edges $-\Delta z/2, \Delta z/2$ of the observation slice (11):

$$\omega_f(\Delta z, t') = \int_{-\Delta z/2}^{\Delta z/2} \sum_{n=0}^{\infty} (-1)^n \left[\operatorname{erfc} \left(\frac{\frac{\Delta z}{2} - z}{\sqrt{4D_f t'}} \right) + \operatorname{erfc} \left(\frac{\frac{\Delta z}{2} + z}{\sqrt{4D_f t'}} \right) \right]$$

Equation S. 8

The equation above is an approximation since it does not account for molecules that leave the observation slice and re-enter it in the “blind time” in between two acquisitions, thus resulting in a underestimation of ω_f . Such underestimation of the fraction of molecules that are still within the observation volume can be compensated for by setting Δz larger than its true value Δz_{true} . To determine how much to increase Δz we performed Monte Carlo simulations varying Δz and the diffusion coefficient over experimentally realistic values. By plotting the corrected Δz_{corr} as function of the input Δz_{true} , we found a simple empirical relationship: $\Delta z_{corr} = \Delta z_{true} + a\sqrt{D}$ where $a = 0.21 \text{ s}^{-1/2}$ (data not shown). Plugging Equations S.4, S.5, and S.8 into Equation S.7 provides the final expression for our model in the theoretical limit of particles localized with infinite precision.

In a realistic scenario a certain localization error σ will widen the distribution of jumps. This can be accounted for by using the procedure developed by Matsuoaka et al.(9) which yields a revised expression for $I(r, t, t')$ (Eq S.4):

$$I_{\sigma}(r, t, t') = \frac{r \Delta r}{2(D_f t' + D_b(t - t') + \sigma^2)} e^{-\frac{r^2}{4(D_f t' + D_b(t - t') + \sigma^2)}}$$

Equation S. 9

Practically, the combination of Equations S.5, S.7, S.8 and S.9 is fit to the experimental data via non-linear least-square minimization to find the best estimates for the parameters D_f, k_{on}^*, k_{off} and Δz . D_b can also be set as a free parameter or fixed to the value for chromatin diffusion obtained from the H2B

data. σ^2 is always set to the value obtained from the histone H2B data. The integrals over the optical axis z (see Equation S.8) and over the free time t' (see Equation S.7) are evaluated numerically through Simpson's integration (Matlab function `quadv`).

We validated the preceding model in both its 2D ($\omega_f = 1$) and 3D versions by fitting simulated single molecule tracking data subject to diffusion and binding interactions over a wide range of the free-parameter space, and found excellent agreement between the model and the simulations (see the “Validation of the displacements histogram kinetic model via numerical simulation” section below).

Multi-component diffusion for free molecules and Brownian diffusion for bound molecules

We extended the displacements histogram model for the case of one bound state but with two species of freely diffusing molecules with diffusing coefficients D_1 and D_2 , both with the same association and dissociation rates to the bound state. If we assume no interchange between the two freely diffusing species, the histogram of displacements can be obtained as a linear combination of the histogram of displacements for each of the species:

$$p_{2D}(r, t)\Delta r = f_1 p_{D_1}(r, t)\Delta r + (1 - f_1) p_{D_2}(r, t)\Delta r$$

Equation S. 10

where f_1 is the fraction of molecules in the first state and $p_{D_1}(r, t)$ and $p_{D_2}(r, t)$ are obtained from Equation S.7 by setting the diffusion coefficients to D_1 and D_2 respectively. Practically, we fit the experimental data with the combination of Eq. S.5, S.7, S.9 and S.10 to obtain estimates for D_1 , D_2 , f_1 , k_{on}^* , k_{off} and Δz . We first estimated the diffusion coefficients D_1 and D_2 by fitting the histogram of displacements obtained for the shortest time interval, $t = \Delta t$, and then fit the whole time-dependent histogram of displacements to obtain estimates for the other parameters.

Validation of the displacements histogram kinetic model via numerical simulation

To verify the validity of our kinetic model we generated simulated data numerically, varying the parameters for D_f , k_{on}^* , k_{off} and Δz over a wide range, and we compared the resulting displacements histograms with our mathematical model. We applied this approach to the validation of the one binding and one diffusing state model.

We performed extensive comparisons between the simulations and the model in the 2D limit ($\Delta z \rightarrow \infty$). Additional testing was performed in 3D to verify the validity of our approximation for the limited thickness of the observation slice. In all cases we found excellent agreement between the simulations and the theory, as fitting the simulated data with our model resulted in estimated parameters that were within 10% of the input parameters of the simulation. Two exemplary fits of the simulated 3D data are provided in Supplementary Fig. 7.

The specifics of the simulation were as follows. We defined the simulation space as a cubic volume with edges equal to $10^3 \mu\text{m}$. At the beginning of the simulation the positions of 10^3 particles were randomly assigned within the simulation space. Each particle had an initial probability of being bound $C_{eq} = k_{on}^* / (k_{on}^* + k_{off})$. The time step dt of the simulation was set equal to 0.4 ms and the simulations were run for $3 \cdot 10^4$ time steps. At every time step, each bound particle had a probability to unbind equal

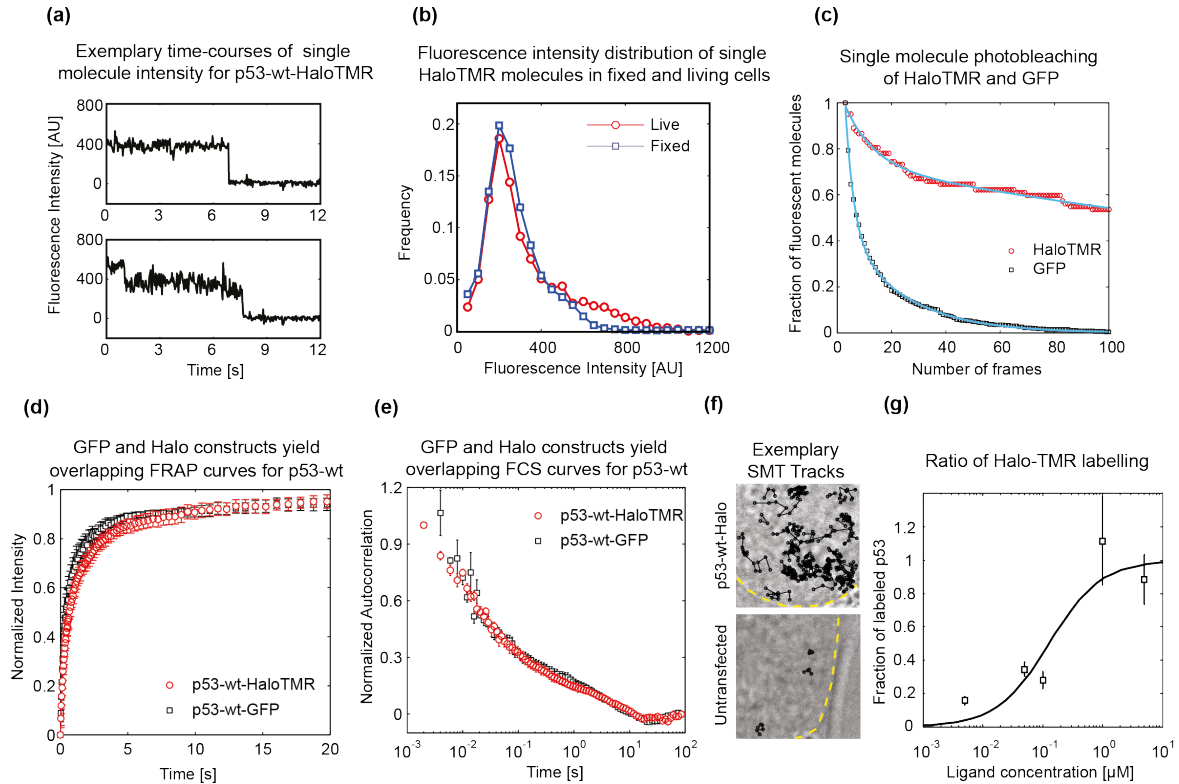
to $1 - \exp(-k_{off}dt)$. Similarly, each free particle had a probability to bind equal to $1 - \exp(-k_{on}^*dt)$. After applying these probabilities to establish the bound and free population at each time step, each molecule in the free population was then assigned a displacement along each of the three axes by random sampling from a normal distribution with standard deviation $\sqrt{2D_f dt}$, where D_f represents the diffusion coefficient of the free molecules. To simulate the finite localization accuracy of the microscope both free and bound molecules were randomly displaced according to a normal distribution with standard deviation $\sqrt{2\sigma}$. We imposed reflection of displacements at the boundary.

Every 100 time steps we extracted the coordinates of the molecules to obtain simulated single molecule tracks. Only particles contained in a volume of thickness Δz around the center of our simulation volume were considered in order to account for the finite thickness of the observation slice.

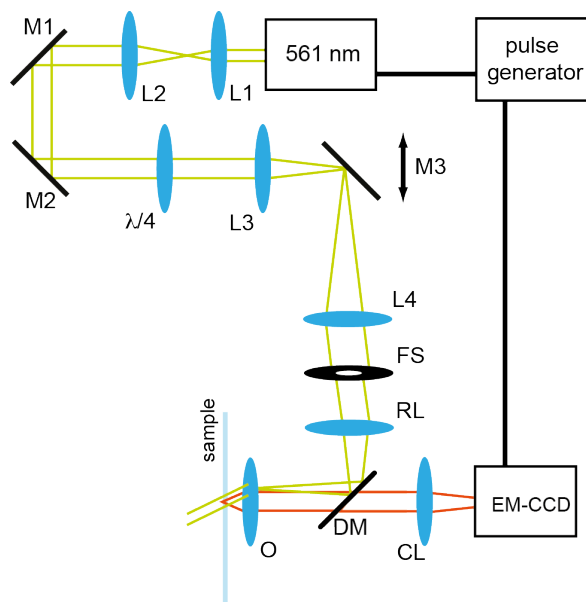
References

1. Los, G.V. and Wood, K. (2007) The HaloTag: a novel technology for cell imaging and protein analysis. *Methods Mol. Biol.*, **356**, 195-208.
2. Rosenke, K., Samuel, M.A., McDowell, E.T., Toerne, M.A. and Fortunato, E.A. (2006) An intact sequence-specific DNA-binding domain is required for human cytomegalovirus-mediated sequestration of p53 and may promote in vivo binding to the viral genome during infection. *Virology*, **348**, 19-34.
3. Tokunaga, M., Imamoto, N. and Sakata-Sogawa, K. (2008) Highly inclined thin illumination enables clear single-molecule imaging in cells. *Nat. Methods*, **5**, 159-161.
4. Crocker, J.C. and Grier, D.G. (1996) Methods of digital video microscopy for colloidal studies. *Journal of Colloid and Interface Science*, **179**, 298–310.
5. Stasevich, T.J., Mueller, F., Michelman-Ribeiro, A., Rosales, T., Knutson, J.R. and McNally, J.G. (2010) Cross-validating FRAP and FCS to quantify the impact of photobleaching on in vivo binding estimates. *Biophys. J.*, **99**, 3093-3101.
6. Mueller, F., Wach, P. and McNally, J.G. (2008) Evidence for a common mode of transcription factor interaction with chromatin as revealed by improved quantitative fluorescence recovery after photobleaching. *Biophys. J.*, **94**, 3323-3339.
7. Michelman-Ribeiro, A., Mazza, D., Rosales, T., Stasevich, T.J., Boukari, H., Rishi, V., Vinson, C., Knutson, J.R. and McNally, J.G. (2009) Direct measurement of association and dissociation rates of DNA binding in live cells by fluorescence correlation spectroscopy. *Biophys. J.*, **97**, 337-346.
8. Crank, J. (1980) *The Mathematics of Diffusion* 2nd ed. Oxford University Press, USA.
9. Matsuoka, S., Shibata, T. and Ueda, M. (2009) Statistical analysis of lateral diffusion and multistate kinetics in single-molecule imaging. *Biophys. J.*, **97**, 1115-1124.
10. Yeung, C., Shtrahman, M. and Wu, X.-lun (2007) Stick-and-Diffuse and Caged Diffusion: A Comparison of Two Models of Synaptic Vesicle Dynamics. *Biophysical Journal*, **92**, 2271-2280.
11. Kues, T. and Kubitscheck, U. (2002) Single Molecule Motion Perpendicular to the Focal Plane of a Microscope: Application to Splicing Factor Dynamics within the Cell Nucleus. *Single Molecules*, **3**, 218-224.

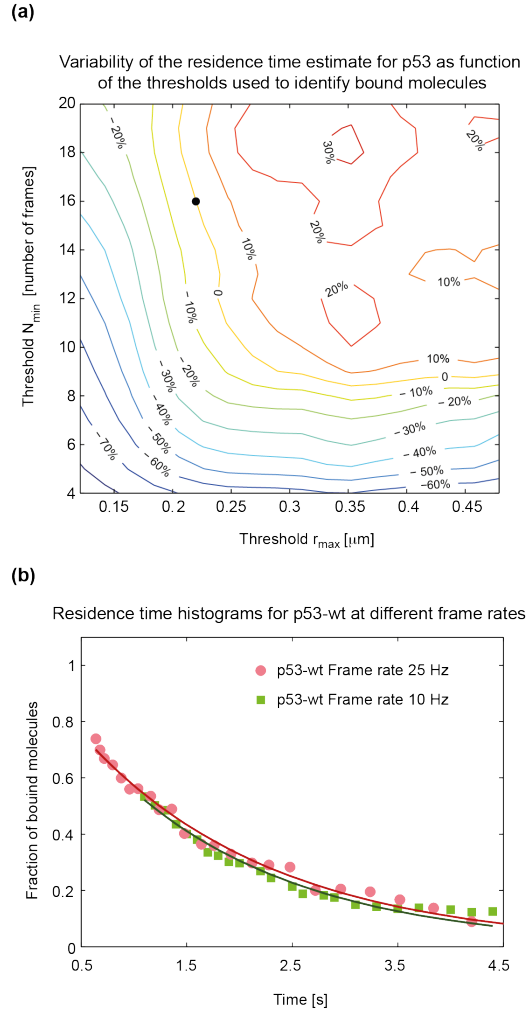
Supplementary Figures.



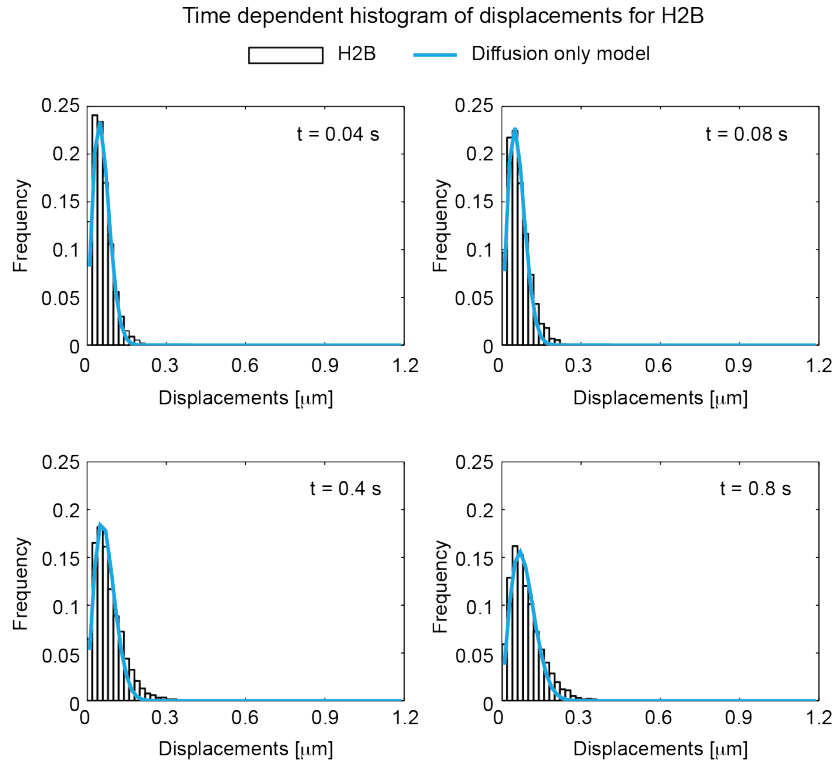
Supplementary Figure 1. Characterization of HaloTag p53-wt photostability and dynamics. (a) The time-course of the fluorescent spots corresponding to the p53-wt Halo fusion proteins in fixed cells displays quantized photobleaching, indicating that individual molecules are observed. Occasionally (< 5%), multiple photobleaching steps (lower panel) are observed, as expected from the tetrameric form of p53. (b) The distributions of single molecule intensities in living and fixed cells overlap, indicating that individual molecules are also observed in the living sample. (c) We quantified the single-molecule photobleaching characteristics of HaloTMR and GFP in fixed cells by counting the number of molecules still fluorescent as a function of the number of frames exposed. The distribution of bleaching times were fit by a double exponential, and the average number of 10 ms exposures before photobleaching was extracted, resulting in 7 time-points for GFP and 230 for HaloTMR. (d) and (e) We verified whether the HaloTag could alter the dynamics of p53 by comparing FRAP (d) and FCS (e) curves for p53-wt-Halo and p53-wt-GFP. The resultant curves show considerable overlap (errorbars s.d. $n > 5$ for FRAP, s.d. $n > 8$ for FCS). (f) The unbound fluorescent ligand is efficiently washed away from the cells as very few single molecules (black circles with black tracks) were detected when adding HaloTMR to untransfected cells. The frame size is $13 \times 13 \mu\text{m}^2$. (g) The fraction of p53 molecules bound by the HaloTMR ligand was calculated by measuring the fluorescence intensity of H1299 nuclei with different amounts of ligand added to the solution. The data were fit by a model $y = 1/(ax + 1)$ to determine by interpolation the fraction of labeled p53 molecules at the ligand concentrations used for FRAP, FCS and SMT (500 nM: 79%, 50 nM: 28% and 5 nM: 4%)



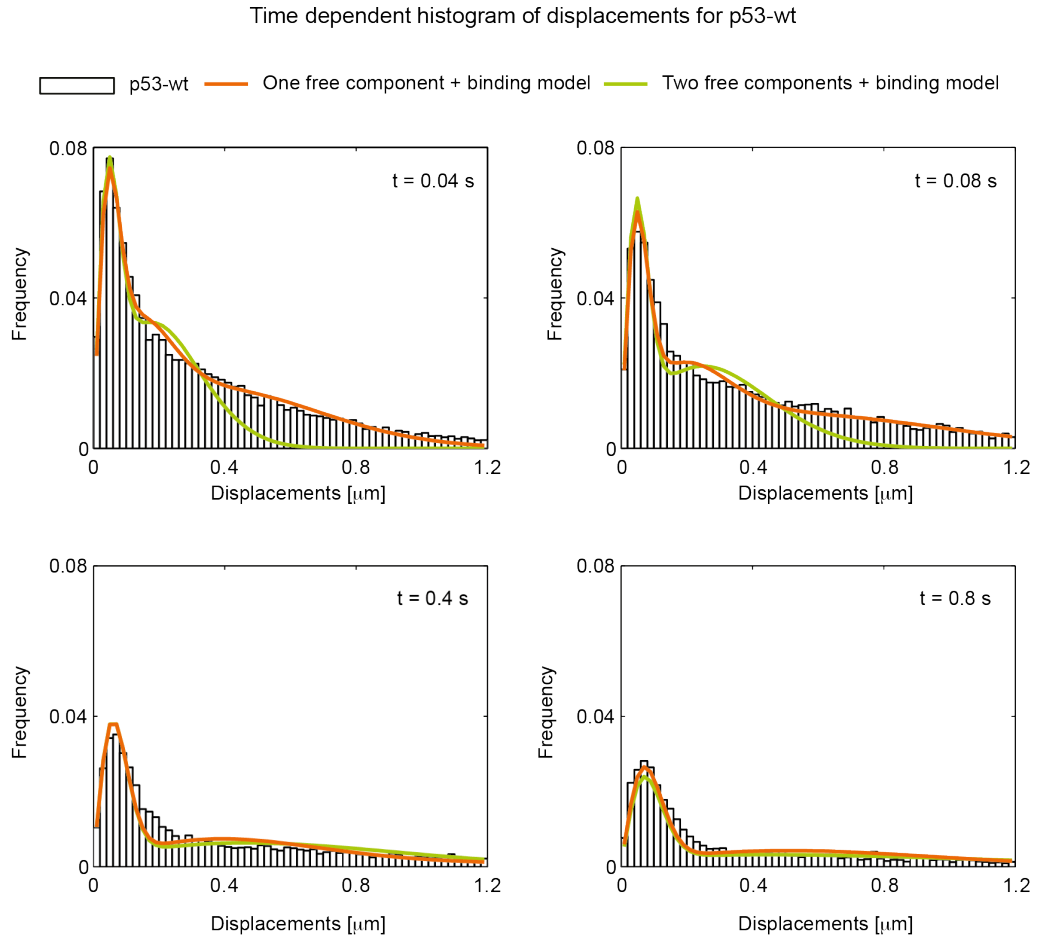
Supplementary Figure 2. Details of the microscope for SMT. The setup for single molecule microscopy we developed is based on an inclined illumination scheme to reduce the background from out-of-focus molecules (3). The collimated beam of a 25 mW, 561 nm DPSS laser (iFlex Mustang 561, Qioptiq) was expanded by means of two lenses (L1, $f = 13\text{mm}$ and L2, $f = 150\text{mm}$) to approximately 7mm in diameter, aligned by a series of mirrors (M1 and M2 in the figure) to the entrance of the microscope and circularly polarized by a quarter wave-plate ($\lambda/4$). A plano-convex lens (L3, $f = 150\text{ mm}$) was used to focus the beam on a translating mirror (M3), placed in a conjugate plane of the back focal plane of the microscope objective. By moving the mirror it is then possible to select the focusing position on the objective back focal plane and, accordingly, the incidence angle of the beam on the sample (green rays), in order to achieve inclined illumination and improved optical sectioning. A second lens (L4, $f = 150\text{ mm}$) collimates the beam, which enters the Olympus IX-81 microscope through an Olympus U-DP dual port, composed of a field stop (FS) which allows adjustment of the illuminated area and a relay lens (RL, $f = 100\text{ mm}$) which focuses the beam on the back focal plane of the imaging lens (O). The fluorescence from the sample (orange rays) is selected using a dichroic mirror (DM, Di01-R561, Semrock, Rochester, NY) and an emission filter (FF-01-617/73, Semrock) and focused on the camera. A pulse generator (BNC-575, Berkeley Nucleonics) is used to synchronize the laser emission with the camera exposure.



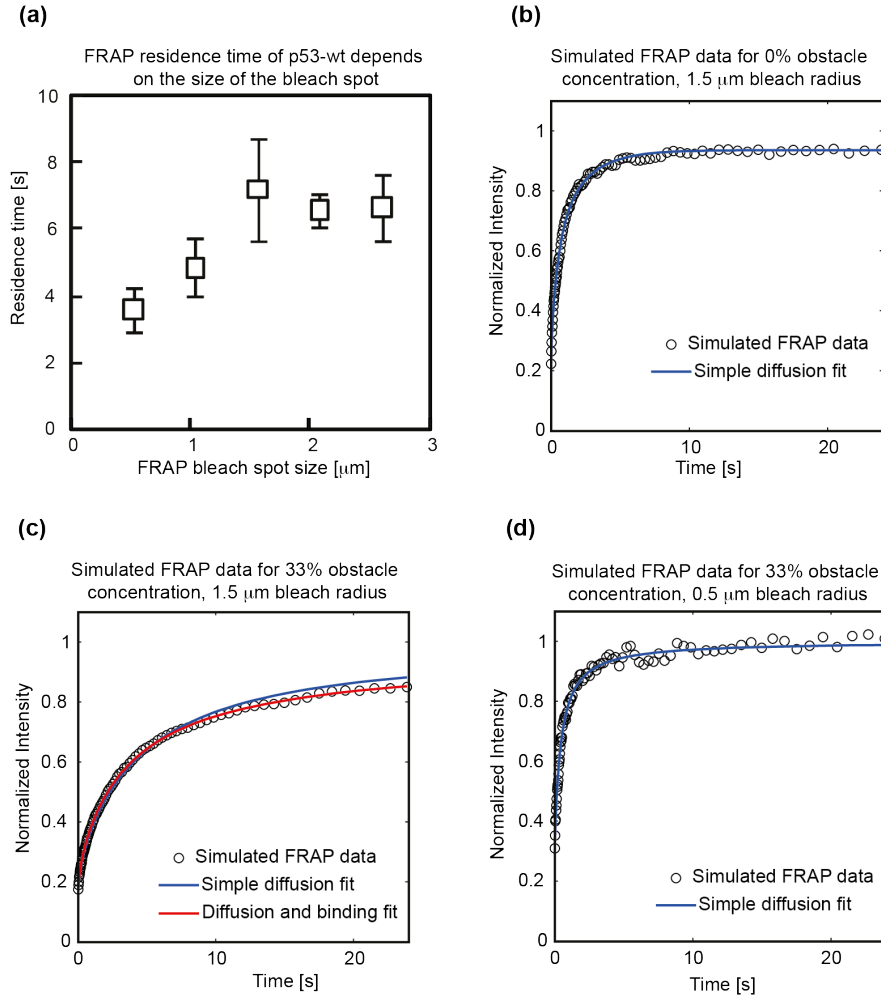
Supplementary Figure 3. Dependence of the measured residence time on the selection of thresholds and on the photobleaching rate (a) The p53 residence time estimate depends only weakly on the choice of the thresholds r_{max} and N_{min} . To evaluate the sensitivity of the residence time estimate to the choice of thresholds used to identify bound molecules, we estimated the p53 residence time for different threshold values. As shown in the contour plot, the error in the estimated residence time is within 30% as long as r_{max} is chosen large enough to include all bound molecule displacements ($>0.25 \mu\text{m}$ in this case) and N_{min} is chosen large enough to exclude the free molecules that transiently exhibit short displacements (>10 frames or 0.4 s in this case). (b) The residence time histogram for p53-wt does not depend on the bleach rate of the tagged molecules. For testing the photobleaching correction procedure, we collected data at two different frame rates (10 Hz and 25 Hz), but kept the same exposure time, thereby generating faster photobleaching at the higher frame rate. We compared the histograms of residence times obtained from the two different frame rates, and found no difference. Both histograms were fit by a single exponential (solid lines) yielding similar residence time estimates, $\tau_b = 1.7 \pm 0.2 \text{ s}$ at 10 Hz and $\tau_b = 1.7 \pm 0.1 \text{ s}$ at 25 Hz. An F-test showed that a double exponential did not significantly improve the fits.



Supplementary Figure 4. Fitting of the H2B displacement histogram at multiple time points. The histogram of displacements obtained by SMT is a two-dimensional surface with displacements on one axis and the time interval t between different points on the trajectory on the other axis. Our kinetic models fit the entire two-dimensional surface. Here we show fits (blue line) to several slices through this surface (specified by different t values). The data are fit with a simple diffusion model with $D = 0.0019 \mu\text{m}^2/\text{s}$. Data acquisition rate was 25Hz.



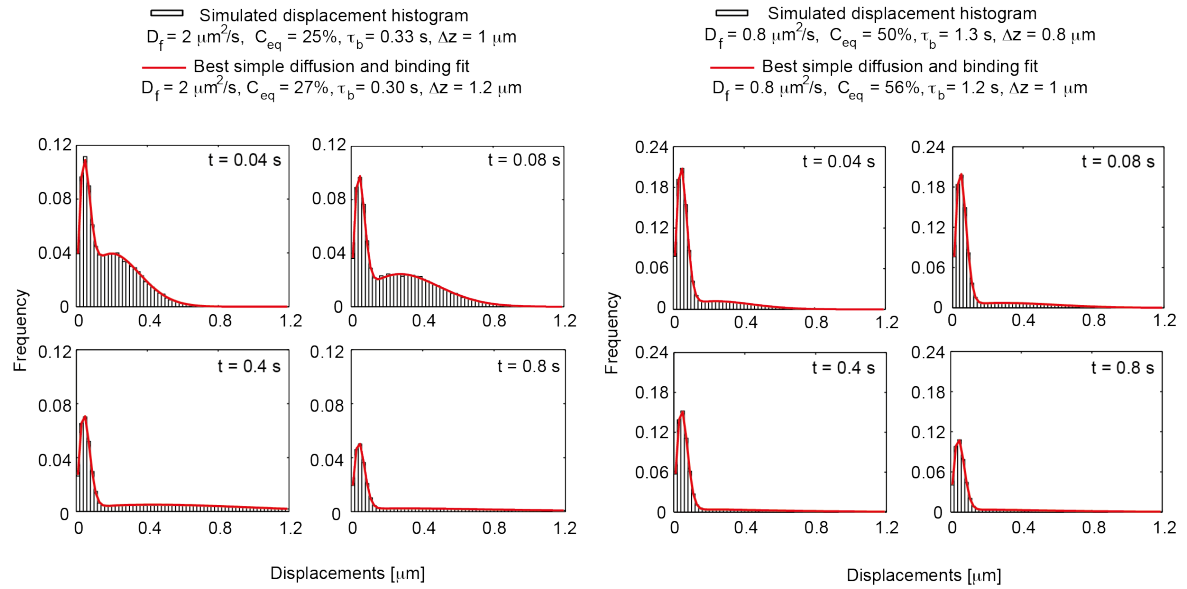
Supplementary Figure 5. Fitting of the p53-wt displacement histogram at multiple time points. Same procedure as in Supplementary Fig. 4, but now applied to p53-wt. Shown are the best fits for the one-component diffusion and binding model (green line) and for the two-component diffusion and binding model (orange line) to cuts through the two-dimensional surface of the p53-wt displacement histogram. Data acquisition rate was 25Hz. See Table 1 for the parameters estimated from these fits.



Supplementary Figure 6. FRAP estimates of the p53-wt residence time depend on the bleach-spot size.

(a) FRAP experiments on p53-wt-Halo performed at different bleach-spot sizes resulted in estimates of the residence time that decreased as the diameter of the bleached region decreased (error bars s.e.m., $n > 15$). A potential explanation is that some deviation from simple diffusion might be misinterpreted as binding by FRAP. To test this hypothesis, we generated FRAP curves by on-lattice 2D Monte Carlo simulations (See Supplementary Methods) assuming a certain concentration of obstacles in the medium and no binding. (b) When no obstacles were present in the simulation, the curves were all well described by the diffusion model. (c) In contrast, simulations with obstacles (33% of the lattice sites were occupied) and a bleach region of 1.5 μm in radius resulted in FRAP curves that were not well described by a simple diffusion model. Rather a diffusion and binding model provided a better fit, resulting in an artificial bound state with a residence time $\tau_b = 7$ s and a bound fraction $C_{eq} = 7\%$. (d) When we performed the same simulations with obstacles, but now with a smaller spot for the bleached region (radius 0.5 μm), we found that a simple diffusion model was sufficient to describe the simulated FRAP curve.

D. Mazza et al., Supplementary Information for
“A benchmark for chromatin binding measurements in live cells”



Supplementary Figure 7. Validation of the SMT kinetic model by simulations. (a) We tested our one-binding state and one diffusing-state model for the SMT displacements histogram by fitting the model to simulated data generated for a wide range of parameters. Two examples are shown here. In all cases the fit yielded parameter estimates that were within 10% of the input parameters of the simulation. D_f is the free fraction, C_{eq} the bound fraction, τ_b the residence time and Δz the depth of field.

Supplementary Tables.

Supplementary Table 1. Estimates of p53 binding rates from kinetic modeling of the histogram of displacements obtained at different data acquisition rates.

	D_1 [$\mu\text{m}^2/\text{s}$]	D_2 [$\mu\text{m}^2/\text{s}$]	f_1 [%]	τ_b [s]	C_{eq} [%]
50 Hz	3.4 ± 0.8	0.66 ± 0.14	48 ± 2	1.72 ± 0.11	17.6 ± 2.6
25 Hz	1.9 ± 0.2	0.21 ± 0.03	58 ± 1	2.2 ± 0.3	17 ± 5
10 Hz	1.44 ± 0.14	0.089 ± 0.16	70 ± 1	2.8 ± 0.8	13 ± 8

Data acquisition rate has no significant effect on the residence time τ_b or bound fraction C_{eq} but does alter the estimated diffusion constants D_1 and D_2 . This may be further evidence for anomalous diffusion. All estimates in the Table were obtained by fitting the p53-wt histogram of displacements with a kinetic model accounting for two free components exchanging with a chromatin bound component. f_1 is the fraction of molecules with diffusion constant D_1 (errors 95% confidence intervals).

Supplementary Movie Legends.

Supplementary Movie 1. p53-wt. The movie shows the first 100 frames of an exemplary unprocessed acquisition for H1299 cells expressing p53-wt, labeled with Halo-TMR. The acquisition rate was 25Hz (displayed at 15Hz) and the frame size $13 \times 13 \mu\text{m}^2$. The position of the nuclear envelope, as determined from a brightfield image of the same field of view, is shown by the yellow line.

Supplementary Movie 2. H2B. The movie shows the first 100 frames of an exemplary unprocessed acquisition for H1299 cells expressing H2B, labeled with Halo-TMR. The acquisition rate was 25Hz (displayed at 15Hz) and the frame size $13 \times 13 \mu\text{m}^2$. The position of the nuclear envelope, as determined from a brightfield image of the same field of view, is shown by the yellow line.